How interface properties control the equilibrium shape of core–shell Fe–Au and Fe–Ag nanoparticles

Ségolène Combettes, Julien Lam, Patrizio Benzo, Anne Ponchet, Marie-José Casanove, Florent Calvo, Magali Benoit

Journal Name

ARTICLE TYPE

Cite this: DOI: 00.0000/xxxxxxxxxx

How interface properties control the equilibrium shape of core-shell Fe-Au and Fe-Ag nanoparticles

Ségolène Combettes[a], Julien Lam[b], Patrizio Benzo[a], Anne Ponchet[a], Marie-José Casanove[a], Florent Calvo[c] and Magali Benoit[a,*]

Received Date
Accepted Date

DOI: 00.0000/xxxxxxxxxx

While combining two metals in the same nanoparticle can lead to remarkable novel applications, the resulting structure in terms of crystallinity and shape remains difficult to predict. It is thus essential to provide a detailed atomistic picture of the underlying growth processes. In the present work we address the case of core-shell Fe-Au and Fe-Ag nanoparticles. Interface properties between Fe and the noble metals Au and Ag, computed using DFT, were used to parameterize Fe-Au and Fe-Ag pairwise interactions in combination with available many-body potentials for the pure elements. The growth of Au or Ag shells on nanometric Fe cores with prescribed shapes was then modelled by means of Monte Carlo simulations. The shape of the obtained Fe-Au nanoparticles is found to strongly evolve with the amount of metal deposited on the Fe core, a transition from the polyhedral Wulff shape of bare iron to a cubic shape taking place as the amount of deposited gold exceeds two monolayers. In striking contrast, the growth of silver proceeds in a much more anisotropic, Janus-like way and with a lesser dependence on the iron core shape. In both cases, the predicted morphologies are found to be in good agreement with experimental observations in which the nanoparticles are grown by physical deposition methods. Understanding the origin of these differences, which can be traced back to subtle variations in the electronic structure of the Au/Fe and Ag/Fe interfaces, should further contribute to the better design of core-shell bimetallic nanoparticles.

1 Introduction

Owing to their multifunctional character, bimetallic nanoparticles (NPs) are being used in an increasing number of applications. Not only do they offer the combined properties of the two metals they are made of, but they can also develop completely new properties through alloying effects. The fields of application of these nanoscale objects are therefore numerous and include catalysis, optics, magnetic recording, drug delivery, hyperthermia, bactericidal actions, etc.[1]

In order to control the properties of these bimetallic nanoparticles, it is essential to master their composition, chemical order and morphology altogether. In particular, obtaining a specific crystalline phase with particular exposed facets is especially desirable for generating specific properties or for use in biomedical applications where molecules must be grafted onto their surface[2]. Whereas composition can be tuned, in principle, by the synthesis conditions, both chemical order and morphology depend on growth kinetics and thermodynamical parameters. For instance, the formation of cubic iron nanoparticles was kinetically favored over the Wulff equilibrium shape under specific growth conditions.[3] In chemical synthesis, the presence and nature of ligands, can also play a prominent role in these characteristics. When two metals are non miscible in the bulk, depending on the growth conditions, chemical orders such as core-shell, multi-shell, Janus but also mixed alloys can be observed at the nanoscale.[1,4–11] The core-shell and Janus chemical orders can also be found for two metals with a propensity to alloy, for specific compositions and synthesis conditions (see[1] and references therein). However, tailoring the type of chemical order obtained for a given combination of metals remains a major technological challenge.

By combining a noble metal such as Au or Ag with a magnetic metal such as Fe, we aim at obtaining nano-objects with both magnetic and optical properties, or to induce exacerbated magneto-plasmonic properties as already observed in other bimetallic NPs.[12–15] Moreover, the cost of such nanoparticles would be reduced compared to nanoparticles made from the more

[a] CEMES, CNRS and Université de Toulouse, 29 rue Jeanne Marvig, 31055 Toulouse, France
[b] Center for Nonlinear Phenomena and Complex Systems, Université Libre de Bruxelles, Code Postal 231, Boulevard du Triomphe, 1050 Brussels, Belgium
[c] Univ. Grenoble Alpes, CNRS, LIPhy, 38000 Grenoble
*Corresponding author: magali.benoit@cemes.fr, +33 5 62 25 79 70.
‡

expensive noble metal alone. Ag and Au share many common features, as they both crystallize in the face-centered cubic (fcc) structure with very similar lattice parameters (4.079 Å for Ag and 4.065 Å for Au[16]), and have also similar surface energies. However, their chemical behavior turns out to be very different, gold being rather inert while silver is highly reactive. Despite these differences, the Fe-Au and Fe-Ag pairs are expected to behave identically. Iron crystallizes in a body-centered cubic structure (bcc) in a large part of its phase diagram. It is strongly immiscible with Ag over the entire phase diagram[17] and is only very weakly miscible with Au[18]. In addition, the surface energies of iron are much higher than those of Au and Ag. Consequently, at equilibrium, the Fe-Au and Fe-Ag systems are likely to form phase separated core-shell (or possibly Janus) nanostructures rather than mixed nanoalloys, iron going preferentially to the core.

Bimetallic Fe-Au nanoparticles have been widely studied and many experimental realizations can be found in the literature. Fe-Au nanoparticles show indeed interesting properties in plasmonics as well as for biomedical applications and catalysis.[19–21] Most of these nanostructures exhibit a core-shell-like configuration with iron in the center and gold forming a protective shell around it. Chemical syntheses usually produce nanoparticles with rather spherical shapes,[22–28] while physical syntheses at high temperature and under high vacuum lead to highly faceted objects with polyhedral (even cubic) iron cores.[29–31] In particular, in previous works, we have shown that Fe@Au nanoparticles synthesized by sequential vapor deposition exhibit a very different morphology depending on the amount of gold deposited on the iron core, the latter changing from a polyhedral shape close to its Wulff shape at equilibrium when the gold shell is 2 to 3 monolayers thick, to a cubic shape when the shell volume is of the same order or larger than the core volume.[31] Note that physical syntheses performed at room or low temperature often lead to rounded shapes[19,32,33] In addition, out-of-equilibrium synthesis conditions can also lead to the formation of metastable nanoparticles made of Fe-Au alloys[34–37] or even to totally unexpected multi-shell nano-objects.[38]

In comparison, Fe-Ag nanoparticles are not as easily obtained by physical routes, most of the literature on these systems referring to chemical production methods.[39–42] In some cases, the reverse chemical order of Ag@Fe with silver in the core was even observed, the iron shell being probably surrounded itself by an iron oxide shell depending on the synthesis conditions.[39] Nonetheless, a few examples have been reported showing that for such systems the Fe core tends to be off-centered and easily oxidized as well, leading to the formation of Fe_3O_4.[43,44] Besides, in-flight cooling experiments have also reported dumbbell-like structures of multiple Fe-Ag nanoparticles encapsulated in a Si shell.[45] Despite being difficult to synthesize in a core-shell configuration, these nanoparticles have shown interesting plasmonic properties[42,44] as well as anti-bacterial activity.[46]

In this contribution, we show that these striking differences between the morphologies of Fe-Au and Fe-Ag nanoparticles are essentially due to dissimilarities between the interface energies of the two noble metals in contact with iron, owing to the different position of the *d* band in their electronic densities of states. In a first section, surface and interface energies computed using DFT are used to parameterize atomistic potentials for the two systems using well-defined many-body components for the pure metals. These potentials are then employed to simulate the growth of bimetallic nanoparticles by depositing atoms on a preexisting iron core and subsequently equilibrating the resulting nanoparticles by Monte Carlo simulations. Two core morphologies are compared, namely the Wulff polyhedron and a cube, being the lowest-energy shapes for bare iron NPs and in the presence of a thick crystalline gold shell, respectively.[47] Besides, these core morphologies were both experimentally observed in Fe-Au core-shell NPs synthesized under quasi equilibrium conditions (high temperature, slow rate deposition, ultra-high vacuum ...).[31] It is found that, for both systems, the NP morphology evolves with increasing amount of metal deposited, but in a radically different way depending on the metal itself. A very good agreement is obtained with experimental observations for both Fe-Ag and Fe-Au NPs, which demonstrates the relevance of our approach. Finally a discussion on the limits and possible extensions of the present computational approach is given as a conclusion.

2 Methodology

The growth of Fe-Au and Fe-Ag nanoparticles was simulated to mimic the experimental protocol of Refs. 29–31 in which Fe@Au nanoparticles have been synthesized by sequential deposition of Fe first, then Au. The morphology of the polyhedral Fe core in the Fe@Au nanoparticles evolves from a Wulff-like polyhedron shape of body-centered cubic metals to a cube shape with increasing amount of deposited gold.[31] We therefore chose to model the atom-wise growth of gold on iron core with prescribed shape (polyhedron or cube). The rather large sizes involved in the experiments preclude the use of DFT to model the nanoparticles. We have therefore chosen to use empirical potentials that are better suited for this purpose. As will be shown below, and in order to reproduce the experimental trends, the potentials must correctly capture some important properties such as the surface and interface energies, and in particular their ordering among the various crystal surfaces.

In the following, we first describe the DFT calculations performed in order to determine surface and interfaces energies in the Fe-Au and Fe-Ag systems. These quantities are then compared with those obtained from different empirical potentials of the literature, motivating our choice to further design a simple but effective model for the interaction between iron and the noble metals.

Spin-polarised DFT calculations were performed using the VASP software,[48,49] with PAW pseudopotentials and the PBE functional.[50] The cutoff energy was set to 600 eV for all calculations and a Methfessel-Paxton smearing parameter of 0.05 eV was used. A Monkshorst-Pack mesh of special k-points was designed to achieve a convergence of the energy of 1 meV/at for each investigated system. Atomic positions were relaxed until the forces became lower than 10^{-2} eV/Å.

Table 1 Surface energies from DFT-PBE calculations, empirical potentials and experiments (values in J/m^2). R^M_{surf} reports the ratio between the (111) or (110) and the (100) surface energies for each investigated metal M.

J/m^2	$\gamma^{\mathrm{Fe}}_{100}$	$\gamma^{\mathrm{Fe}}_{110}$	R^{Fe}_{surf}	$\gamma^{\mathrm{Au}}_{100}$	$\gamma^{\mathrm{Au}}_{111}$	R^{Au}_{surf}	$\gamma^{\mathrm{Ag}}_{100}$	$\gamma^{\mathrm{Ag}}_{111}$	R^{Ag}_{surf}
DFT-PBE	2.478	2.428	0.98	0.873	0.734	0.84	0.814	0.741	0.91
EAM-LJ	2.009	1.901	0.95	1.061	0.939	0.89	0.938	0.860	0.92
EAM Calvo *et al.*[47]	2.009	1.901	0.95	1.061	0.939	0.89	-	-	-
EAM Zhou *et al.*[51]	1.711	1.429	0.84	1.023	0.900	0.88	1.141	1.035	0.91
Gupta Vernières *et al.*[38]	1.705	1.531	0.90	0.610	0.552	0.90	-	-	-
Exp.	-	2.417[52] 2.475[53] 2.550[56]	1.0[54]	-	1.5[52]	0.84[55]	-	1.24[52]	-

2.1 DFT surface energies

The surface energies were evaluated using periodic models made of slabs of a given number of monolayers (MLs) separated by 15 Å of vacuum in the z direction. The surface energy is then obtained using:

$$\gamma = \left[E^{\mathrm{slab}} - N^{\mathrm{at}} E^{\mathrm{bulk}}_{\mathrm{at}}\right] / 2A \qquad (1)$$

where E^{slab} is the total energy of the slab containing N^{at} atoms, $E^{\mathrm{bulk}}_{\mathrm{at}}$ the bulk atomic energy and A the surface area. The numbers of layers in the slabs were increased until γ was converged within 10 mJ/m^2.

The results obtained from the DFT-PBE calculations are given in Table 1. As can be seen from this table, the PBE functional underestimates the surface energies of Au(100) and Au(111) with respect to the experimental values (≈1.5 J/m^2, Ref. 52). However the ratio $R^{Au}_{surf} = \gamma_{111}/\gamma_{100} = 0.84$ between the two corresponding energies is in good agreement with the experimental estimate of 0.84 obtained using the Wulff theorem on gold NPs observed by HR-TEM.[55] Regarding now the Ag surface energies, the experimental value for the Ag(111) surface is around 1.24 J/m^2 (Ref. 52), which is also underestimated by the PBE functional but the obtained ratio between the two surfaces $R^{Ag}_{surf} = \gamma_{111}/\gamma_{100} = 0.91$ achieved from a Wulff shape analysis of silver clusters is also in agreement with experiments performed on silver clusters (0.97)[57]. Conversely, for iron, the Fe(100) and Fe(110) surface energies as well as their ratio are in very good agreement with experiment using the PBE functional (2.417 J/m^2 from Ref. 52, 2.475 J/m^2 from Ref. 53, and 2.550 J/m^2 from Ref. 56).

2.2 DFT interface energies

For the determination of the interface energies between iron and the noble metals, model systems consisting of a slab of M layers of X=Au or Ag in contact with a slab of N layers of Fe were used. Periodic boundary conditions were employed in the x, y and z directions and the two slabs were separated from their images by adding 15 Å of extra vacuum in the z direction (Fig. 1).

Depending on the epitaxial relationship between the orientations of the two slabs, a mismatch can exist at the interface between the two crystals, which leads to some accumulation of elastic energy in the slabs and contributes to the surface and interface stresses. In the following, we only consider the case where the Fe slab is at its equilibrium lattice constant and the Au(Ag) slab is in epitaxial contact with its surface, thus undergoing most of the deformation due to lattice mismatch. This approximation is justified by the sequential growth of the NPs, where the iron core is formed first.

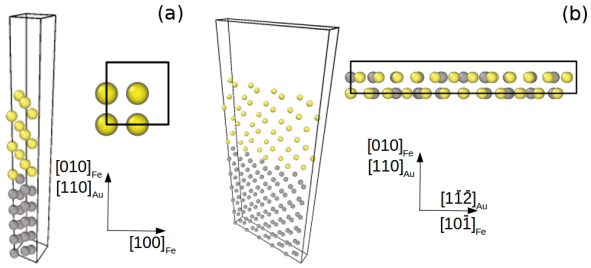

Fig. 1 Periodic simulation models used to compute the X/Fe (X=Au or Ag) interface energies, 3D and top views (shown here for X=Au). (a) X(100)/Fe(100); (b) X(111)/Fe(110). Fe atoms are depicted in gray, Au atoms in yellow. The axes refer to the top views.

Under such circumstances, the total energy of the system reads:

$$\begin{aligned} E_{\mathrm{tot}} &= N^{\mathrm{Fe}}_{\mathrm{at}} E^{\mathrm{Fe}}_{\mathrm{bulk}} + \gamma^{\mathrm{Fe}} A^{\mathrm{Fe}} + N^{\mathrm{X}}_{\mathrm{at}} \left(E^{\mathrm{X}}_{\mathrm{bulk}} + u^{\mathrm{X}}_{\mathrm{elas}} V^{\mathrm{X}}_{\mathrm{at}}\right) \\ &+ \left(\gamma^{\mathrm{X}} + 2\sigma^{\mathrm{X}}\varepsilon_{\parallel}\right) A^{\mathrm{X}} + \left(\gamma^{\mathrm{int}} + 2\sigma^{\mathrm{int}}\varepsilon_{\parallel}\right) A^{\mathrm{int}} \qquad (2) \end{aligned}$$

where $N^{\mathrm{Fe}}_{\mathrm{at}}$ and $N^{\mathrm{X}}_{\mathrm{at}}$ are the numbers of Fe and X atoms in the slabs, respectively, $E^{\mathrm{Fe}}_{\mathrm{bulk}}$ and $E^{\mathrm{X}}_{\mathrm{bulk}}$ being the bulk atomic energies. The latter have been computed with VASP using the same setup (cutoff energy, pseudopotentials, optimized k-point grid, smearing etc.) in a unit cell approach. γ^{Fe}, γ^{X} and γ^{int} denote the surface energies and interface energies, while $u^{\mathrm{X}}_{\mathrm{elas}}$ is the elastic energy per unit volume in the X slab, $V^{\mathrm{X}}_{\mathrm{at}}$ the X atomic volume and A^{Fe}, A^{X}, and A^{int} the Fe and X surface areas, and the interface area at equilibrium, respectively. Finally, σ^{X} and σ^{int} are the X surface and interface stress along the x and y directions and $\varepsilon_{\parallel}$ the in-plane strain. Note that here we considered identical strains and stresses along the two in-plane directions x and y. While this is true in the case of the X(100)/Fe(100) interface, it does not hold for the X(111)/Fe(110) interface. However, since the stresses will not be explicitly evaluated in this work, we will keep this simplified notation in the following.

By subtracting the total energy of the Fe slabs, we end up with a quantity that depends linearly on the number of atoms in the X

Table 2 Interface energies and wetting parameter S from DFT-PBE calculations and empirical potentials (values in J/m^2). $R_{int}^{X/Fe} = \gamma_{111/110}^{X/Fe}/\gamma_{100/100}^{X/Fe}$ is the ratio between the two interface energies.

	$\gamma_{100/100}^{Au/Fe}$	S	$\gamma_{111/110}^{Au/Fe}$	S	$R_{int}^{Au/Fe}$	$\gamma_{100/100}^{Ag/Fe}$	S	$\gamma_{111/110}^{Ag/Fe}$	S	$R_{int}^{Ag/Fe}$
DFT-PBE	0.378	-1.227	0.700	-0.994	1.85	0.996	-0.668	1.071	-0.643	1.07
EAM-LJ	0.260	-0.688	0.662	-0.300	2.55	0.778	-0.293	0.858	-0.183	1.10
EAM (Calvo *et al.*[47])	0.267	-0.681	0.762	-0.200	2.84	-	-	-	-	-
EAM (Zhou *et al.*[51])	-0.698	-1.386	-0.261	-0.790	0.37	0.053	-0.517	0.387	-0.007	7.30
Gupta (Vernières *et al.*[38])	0.996	-0.099	0.822	-0.157	0.83	-	-	-	-	-

slab, i.e. on the number of X monolayers:

$$\begin{aligned}\Delta E = E_{\text{tot}} - E_{\text{slab}}^{\text{Fe}} &= N_{\text{at}}^{\text{X}}\left(E_{\text{bulk}}^{\text{X}} + u_{\text{elas}}^{\text{X}} V_{\text{at}}^{\text{X}}\right) + \left(\gamma^{\text{X}} + 2\sigma^{\text{X}}\varepsilon_{\parallel}\right)A^{\text{X}} \\ &+ \left(\gamma^{\text{int}} + 2\sigma^{\text{int}}\varepsilon_{\parallel}\right)A^{\text{int}} - \gamma^{\text{Fe}}A^{\text{Fe}} \qquad (3)\end{aligned}$$

By computing ΔE for an increasing number of X monolayers, we can deduce the intercept of the regression, which is given by:

$$\left(\gamma^{\text{X}} + 2\sigma^{\text{X}}\varepsilon_{\parallel}\right)A^{\text{X}} + \left(\gamma^{\text{int}} + 2\sigma^{\text{int}}\varepsilon_{\parallel}\right)A^{\text{int}} - \gamma^{\text{Fe}}A^{\text{Fe}}. \qquad (4)$$

The value of γ^{Fe} at equilibrium is known (Tab. 1) and $\tilde{\gamma}^{\text{X}} = \left(\gamma^{\text{X}} + 2\sigma^{\text{X}}\varepsilon_{\parallel}\right)$ can be easily accessed from the surface energy of the X slab subject to the same deformation than in the interface model. It is then straightforward to obtain $\tilde{\gamma}A^{\text{int}}$ where $\tilde{\gamma} = \left(\gamma^{\text{int}} + 2\sigma^{\text{int}}\varepsilon_{\parallel}\right)$. Note that neither the value of A^{int}, the area of the interface at equilibrium, nor the value of σ^{int}, are known a priori. We can nevertheless estimate $\tilde{\gamma}$ in the two limiting cases of $A^{\text{int}} = A^{\text{Fe}}$ and $A^{\text{int}} = A^{\text{X}}$.

For the X(100)/Fe(100) interface, we used the same models as described in Refs.[58,59] to compute the interface energy (Fig. 1(a)). For the X(111)/Fe(110) interface, the epitaxial relationship is much more complex than for X(100)/Fe(100) and follows the Nishiyama-Wassermann relationship.[60] In the [010]Fe//[110]X direction, the same coherent epitaxy as for the X(001)/Fe(001) interface is considered. In the $[10\bar{1}]$Fe//$[1\bar{1}\bar{2}]$X direction, a semi-coherent approach is required. As ensuring an ideal coincidence lattice in this direction would require too large a system to be conveniently modeled in DFT with periodic boundary conditions, we chose to model this interface with a smaller coincidence lattice, as illustrated in Fig. 1(b). This approach has already been used successfully by Lu *et al.* for the Ag(111)/Fe(110) interface.[61] Two different sizes along the [110] direction have been tested for the Au(111)/Fe(110) case: 8 Au and 10 Fe cells (8×10), or 7 Fe and 9 Au cells (7×9). A lower interface energy by -67 meV was found with the 8×10 coincidence network with respect to the 7×9 one, so we chose to use the 8×10 network hereafter. We also tested the epitaxial position of Au atoms on top of the Fe cell (hollow position or bridge position) and found that atoms at hollow sites relaxed to bridge positions. After optimization, the interface rearranged with the creation of an interface dislocations network which helps to reduce the total energy of the system, the accommodation of the Au and Fe networks generating two dislocations per coincidence lattice cell (8x10 or 7x9) (see Supp. Info). Note that at the interface, the z-displacements of the Fe atoms are different on either side of each dislocation, even when the lattice comprises an even number of atoms (8x10). The same model has then been used to study the Ag(111)/Fe(110) interface and the calculated interface energy of 1.071 J/m2 (Tab. 2) is consistent with that obtained by Lu *et al.* (1.18 J/m2)[61] Here as well, the interface dislocations network is made of two dislocations per coincidence network cell with the same dissymmetry of the Fe displacements on either side of each dislocation as for Au(111)/Fe(110) (see Supp. Info).

The values of DFT interface energies $\tilde{\gamma}$ were obtained with a number of 12 Fe MLs and using a linear regression between 4 and 7 MLs of Au or Ag. Only values computed for $A^{\text{int}} = A^{\text{Fe}}$ are shown in Table 2. The values obtained with $A^{\text{int}} = A^{\text{X}}$ are higher by ≈40 to 90 meV, but the ratio between the two interface energies is exactly the same, whatever the reference used. The ratio $R_{int}^{X/Fe}$ given in Tab. 2 corresponds to the ratio between the two interfaces, $R_{int}^{X/Fe} = \gamma_{111/110}^{X/Fe}/\gamma_{100/100}^{X/Fe}$. One can note that, while the surface energies of Au and Ag are close to each other, their interface energies with Fe are very different. First, the two interfaces energies $\gamma_{100/100}^{Ag/Fe}$ and $\gamma_{111/110}^{Ag/Fe}$ are much higher than the corresponding values involving Au. Second, their ratio is also very different, varying from 1.07 in the case of Ag/Fe to 1.85 in the case of Au/Fe.

The important difference between the Au/Fe and Ag/Fe interface energies is essentially due to electronic effects since the two systems undergo a similar lattice mismatch. The electronic properties of the interfaces were thus analyzed for the two investigated systems. In Fig. 2, the densities of states projected on atoms at the interfaces are depicted. For the two different interfaces X(100)/Fe(100) and X(111)/Fe(110), the Fe-projected DOS are similar whether the metal in contact is Au or Ag (light and dark blue lines). Conversely, the Au- and Ag-projected DOS are quite different, in particular between −2.5 eV and −1.0 eV where there are more Au states than Ag states, the d band of gold being much wider than that of Ag. This is true for both interfaces and implies a stronger coupling between Au and Fe than between Ag and Fe, resulting into a lower interface energy for the former. This effect has already been observed on atomic state densities in small clusters of Fe-Au and Fe-Ag[62] and can be traced back to the relativistic nature of gold. For this element, the high velocity of core electrons surrounding the heavy nuclei increases their effective mass. As a consequence of special relativity, the s electrons (and to a lesser extent the p electrons) are in smaller orbitals and are more strongly bound than if these effects were absent, while the d electrons are less bound and occupy larger orbitals. This

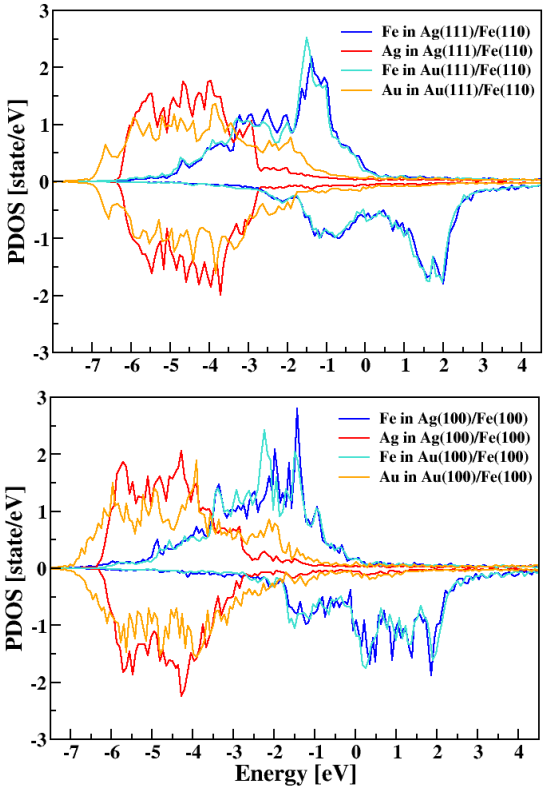

Fig. 2 Projected electronic density of states (PDOS) on selected atoms at X/Fe interfaces (positive and negative values correspond to spin up and spin down, respectively). Upper graph: atoms at the X(111)/Fe(110) interface; Lower graph: atoms at the X(100)/Fe(100) interface.

effect is much stronger for gold than for silver, due to the filling of the 5*d* band which incidentally also accounts for its higher oxidation states and explains its better resistance to oxidation.[63] As discussed below, this result will have important consequences on the morphology of the Fe-X nanoparticles.

2.3 Empirical modeling at the atomistic level

For the pure metals, numerous empirical potentials are available in the literature, some of which give surface energies in good agreement with the experimental values.[64–66]

For the Fe-Au and Fe-Ag interactions, however, only very few potentials have been proposed despite the importance of the elements involved. The EAM potential developed by Zhou *et al.*[51] tends to favor solid solutions for Fe-Au NPs,[47] which is manifested here as a negative interface energy for the two interfaces investigated (see Tab. 2). Although slightly better, the interface energies obtained with the Fe-Ag potential from the same authors[51] are much too small compared to the DFT calculated values.

In our previous work, the EAM potential of Mendelev and coworkers for iron[65] and the potential of Chamati and Papanicolaou for gold[67] were combined together, keeping a many-body character for the Fe-Au interactions whose parameters were adjusted to reproduce various structural and energetic properties of clusters and bulk intermetallics.[47] This model gave interface energies in very good agreement with the DFT reference values for the two interfaces investigated in this work (see Tab. 2). However, in using it for the growth of Fe@Au nanostructures, it was also found to favor another interface between Fe(100) and Au(111) that is not experimentally observed and whose interface energy calculated by DFT is much higher than that of the two other interfaces. Because of this unexpected discrepancy, we have chosen not to use this potential in the present study.

Another Fe-Au potential of the Gupta type was recently used by Vernières and coworkers[38] who simulated the formation of multi-shell Fe-Au nanoparticles. While this potential yields surface energies that are correctly ordered, the interface energies are poorly described, the relative stabilities being inverted with respect to DFT values (see Tab. 2). This potential is therefore not suited either for the present investigation. Finally, the work of Akbarzadeh *et al.*,[68] also based on Gupta-like potentials but using different parameters as those employed by Vernières *et al.*, showed that the alloy configuration is most favorable when the composition is Fe-rich, which is not the expected result at equilibrium.

Besides interface energies, it can be interesting to have some information on the wetting of the X metal on iron. Here we calculate a wetting parameter S defined as:[60]

$$S = \gamma^{\mathrm{X}} + \gamma^{\mathrm{int}} - \gamma^{\mathrm{Fe}}. \quad (5)$$

Note that a small error on the value of S is expected here because we use $\tilde{\gamma}$ instead of γ^{int} owing to the value of the interface stress not being known. However we estimate this error to be of the order of a few percents of the value of the wetting parameter.[58] If S is negative and large in magnitude, then the X metal will have a strong tendency to spread over the Fe surface upon 2D growth. If S is positive but small in magnitude, the metal X will have a tendency to form islands on the Fe surface. Therefore, besides a correct ordering among interface energies, it is also important for the empirical potentials to reproduce the wetting parameters obtained from DFT calculations. From Tab. 2, we note that the DFT calculations give a large and negative S for Au on Fe, which indicates that Au has a strong tendency to wet Fe for both interfaces considered. Regarding Ag on Fe, S is also negative for both interfaces, although smaller in magnitude than for Au on Fe. All the considered empirical potentials give negative wetting parameter values for the investigated interfaces. However, some of them give much lower values than those obtained from DFT.

As will be shown below, the interface energy appears to be one of the driving forces for the observed core-shell morphologies in both Fe-Au and Fe-Ag nanoparticles. In view of the difficulties shown by the above listed existing potentials, we turned to another strategy by designing Fe-Au and Fe-Ag potentials based on well-defined ingredients for the pure elements but simple pairwise additive interactions between unlike elements, adjusting the parameters to reproduce as best as possible the interface energies determined above from DFT, leaving aside other structural or energetic features. For simplicity, the Lennard-Jones (LJ) interaction potential was considered for this purpose. Note that LJ potentials have already been used successfully to model bimetallic nanostructures.[69] Using LJ potentials for the interactions between un-

like elements„ we purposely focus on phase-separated structures instead of alloyed phases. This is motivated by the mostly immiscible nature of both gold and silver with Fe [17,18], the alloyed structures being found to be unfavorable. [47]

For the Fe-Fe, Au-Au and Ag-Ag interactions, we chose the Mendelev, [65] Chamati [67] and Williams [66] potentials, respectively. The two LJ parameters of distance (d) and energy (E_0) were adjusted to reproduce the DFT reference data, especially the ratio between the interface energies. The results obtained with the EAM-LJ potentials thus optimized are reported in Table 2. As can be seen, good agreement could be reached for the interface energies and their ratio for Fe-Au using $E_0 = 0.2$ eV and $d = 2.3$ Å and, for Fe-Ag, using $E_0 = 0.14$ eV and $d = 2.6$ Å. The sign of the wetting parameter S is also obtained satisfactorily although the magnitude is generally lower than in DFT. In addition the z displacements of Fe atoms observed at both Au(111)/Fe(110) and Ag(111)/Fe(110) interfaces display the same behavior as obtained with DFT (see Supp. Info).

2.4 Modeling the growth of core-shell nanoparticles

In order to mimic the growth processes taking place in the sputtering experiments under high vacuum and high temperature of Refs. 29–31, the sequential deposition of atoms on an already formed Fe core was simulated at the atomistic level of details. Two different core shapes were used, namely a Wulff polyhedron, with a majority of (110) and (100) facets as expected for the equilibrium shape of a Fe bare nanoparticle, and a cube. While these two core shapes resemble very strongly those experimentally observed in the case of the Fe-Au system, [29–31] there is presently no experimental evidence for the occurrence of these morphologies in the Fe-Ag system. Nevertheless, the comparison necessarily holds in the limit of the bare iron particle, and the hypothesis that Ag would be deposited on a Wulff-type iron core in vacuum thus seems quite reasonable.

Energetic comparison between structures is better achieved for identical numbers of atoms, hence limited numbers of iron atoms had to be removed from the core seeds because the Wulff and cube growth series do not share the same magic numbers of full geometric shell completion. In order not to favor either of the two structural types, we arbitrarily imposed a number of iron atoms equal to 1000 in the core, removing as many outer atoms as necessary for both structural types. The systems were then equilibrated using molecular dynamics trajectories at 300 K before subsequent local optimization using conjugate gradient. Such a low relaxation temperature was chosen to prevent from excessive rearrangements of the core itself. The two core seeds containing exactly 1000 atoms and obtained with this computational protocol are depicted in Figure 3. Due to the removed atoms, a few defects remain at the surface of the two cores and the so-called cubic core is more like a square cuboid.

The deposition of several X=Au or Ag atoms on these Fe cores was simulated using a Monte Carlo growth scheme in which a population of candidate structures with M members is generated and maintained. Initially, the bare iron core is replicated M times to generate this population. Then, a number N_{add} of single atom additions are randomly attempted on any configuration from the pool drawn with uniform probability, the structures obtained being locally relaxed to produce as many candidate configurations for the next step of the sequence.

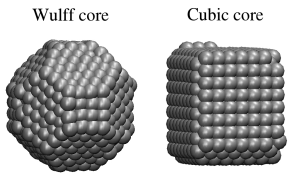

Fig. 3 The two shapes of the iron core on which noble metals were deposited. Left: Wulff-like morphology; right: cubic-like morphology.

From the knowledge of the energy E_i of each optimized structure, its statistical weight p_i is determined from its Boltzmann factor at temperature T_{growth}. This structure is then replicated in the subsequent pool proportionally to $M \times p_i$, keeping the total number of members as constant and equal to M. Doing so, most structures with a high energy are simply ignored, while the lowest-energy structures among the set can be present in multiple copies. The process is then iterated until the number of X atoms reaches the desired value. In practice, we used $T_{\mathrm{growth}} = 1000$ K, $M = 3$ and $N_{\mathrm{add}} = 2000$.

Once entire growth sequences were obtained with the above described procedure, some of the intermediate structures selected along the way were subject to independent equilibration and relaxation using canonical Monte Carlo simulations at 800 K with 50 000 steps. Monte Carlo simulations have the advantage over molecular dynamics to be less sensitive to slow diffusion kinetics associated with energy barriers, allowing equilibrium structures to be produced more effectively. We note though that the rather high temperature of the studied systems (T = 800 K), makes kinetic barriers to be rather unlikely in practice.

3 Fe-Au nanoparticles

Fig. 4 shows the evolution of the energy per atom of the nanoparticle as a function of the ratio between the number of deposited Au atoms and the number of Fe atoms (at constant number of Fe atoms), for the Wulff and cube core morphologies and after their Monte Carlo relaxation at 800 K. Selected configurations, indexed by numbers in Fig. 4, are depicted in Figs. 5 and 6, for the Wulff and cube core shapes, respectively.

As expected, the Wulff polyhedron being the equilibrium shape for bare iron NP, its energy is lower than the corresponding value for the bare cubic particle. When Au atoms start to be deposited, the energy of the two systems increases concomitantly but shows a different behavior from $N_{\mathrm{at}}^{\mathrm{Au}}/N_{\mathrm{at}}^{\mathrm{Fe}} \approx 0.3$. While the energy increases monotonously with the amount of deposited Au for the Wulff core case, it displays a sharp decreases at $N_{\mathrm{at}}^{\mathrm{Au}}/N_{\mathrm{at}}^{\mathrm{Fe}} \approx 0.5$ for the cubic core case, which leads to the two energy curves crossing each other.

In Figure 5, the Wulff-type core NP first exhibits an incomplete wetting monolayer of Au (configuration **1**), the incomplete character being simply due to the lack of gold to cover the entire Fe core in the initial stage of growth. Note that despite the

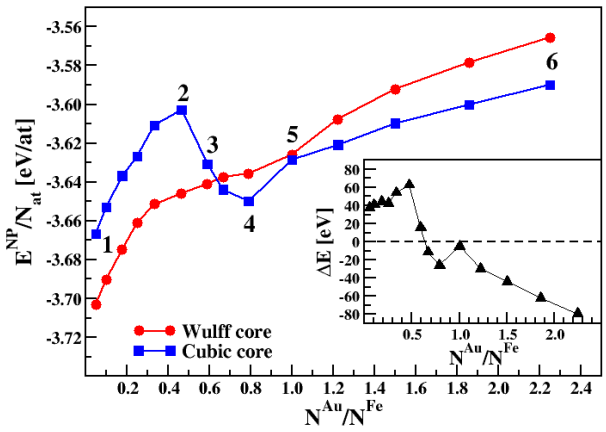

Fig. 4 Energy per atom as a function of the N_{at}^{Au}/N_{at}^{Fe} ratio (for $N_{at}^{Fe} = 1000$), for the Wulff-like (red circles) and cube-like (blue squares) Fe core shapes, after Monte Carlo relaxation at 800 K. Inset: energy difference (in eV) $\Delta E = E_{cube} - E_{Wulff}$ between the two types of nanoparticles.

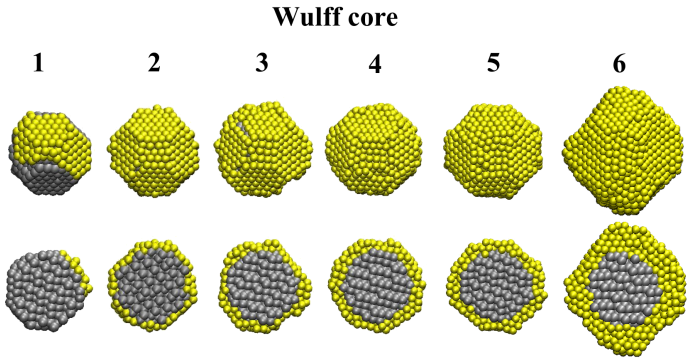

Fig. 5 Selected configurations of the Fe-Au nanoparticles with a Wulff Fe core, taken along the growth path (Fig. 4). Upper panel: outside views; lower panel: only back halves shown.

random spatial distribution of the Au atoms added at the core surface, the growth proceeds asymmetrically, concomitantly with the energetic benefit of creating Au-Au interactions relative to the weaker Fe-Au bond. In addition, because the growth proceeds as to maximize cohesion, facets are covered before edges and eventually vertices.

As the number of Au atoms increases, the energy of the system increases monotonically until N_{at}^{Au}/N_{at}^{Fe} reaches ≈0.3, then shows a slight inflexion which can be explained by the filling of the gold monolayer around the iron core (configuration **2** in Fig. 5). This wetting layer is consistent with the value of the wetting parameter for this system (see Tab. 2) that indicates a strong tendency for gold to cover iron with 2D layers. The energy cost of the sum of Au/Fe interfaces and Au surfaces is therefore lower than that of bare iron surfaces. As N_{at}^{Au}/N_{at}^{Fe} reaches ≈0.4, the system displays a homothetic Au shell around the Fe core (configurations **3** and **4** in Fig. 5), then pyramids on the Fe(100) faces of the Wulff core develop, the height of which increases with the number of deposited Au atoms (configuration **5** and **6** in Fig. 5).

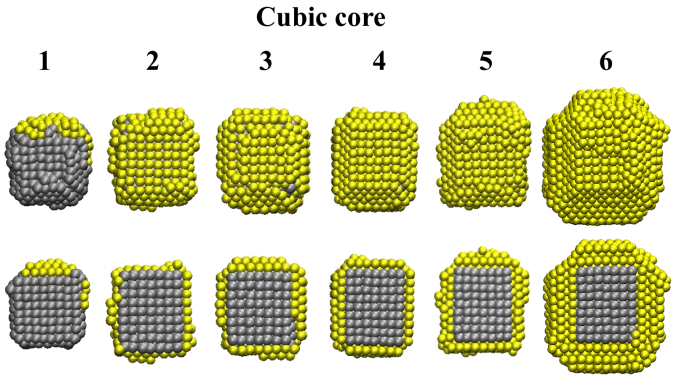

Fig. 6 Selected configurations of the Fe-Au nanoparticles with a cubic Fe core, taken along the growth pathway (Fig. 4). Upper panel: outside views; lower panel: only back halves shown.

In Figure 6, configurations for the cubic core NP are shown for selected numbers of deposited Au atoms along the growth pathway. Configuration **1** exhibits an incomplete wetting monolayer of Au since there is not enough gold to cover the cube entirely. As the gold/iron ratio N_{at}^{Au}/N_{at}^{Fe} exceeds approximately 0.47, the energy starts decreasing in the cubic core system. At this stage, the Fe cube is almost totally coated by a Au monolayer, except on the corners and edges. As for the Wulff core case, this is consistent with the value of the wetting parameter for this system. In configuration **2**, some parts of the Fe(100) cube faces begin to be covered by Au bilayers. Then the configurations with a partial or a complete second layer (**3** and **4** respectively) provide a significant reduction of the energy per Au atom with respect to configuration **2**. When the ratio N_{at}^{Au}/N_{at}^{Fe} reaches about 0.8, we find a minimum in the energy curve of the cubic core NP, which corresponds to a complete coverage of the Fe cube by Au bilayers (configuration **4** in Fig. 6) and indicates a special stability for the bilayer-coated cubic core particles. As the ratio N_{at}^{Au}/N_{at}^{Fe} exceeds approximately 0.8, the energy curve increases monotonically with the number of deposited atoms. From this point, the second Au monolayer provides a suitable ground for the further development of truncated Au pyramids whose side facets are of the Au(111) type (configurations **5** in Fig. 6). For large Au shells (configuration **6** in Fig. 6), we find a core-shell chemical order of symmetrical shape with truncated pyramids on each of the cube facets.

Comparing the results of the growth simulations obtained on the two core shape types, the following features can be noted. When the ratio N_{at}^{Au}/N_{at}^{Fe} is lower than about 0.6 (configurations **1**, **2** and **3** in Figs. 6 and 5), the energy of the Wulff-core NP is lower than that of the cubic-core NP because the amount of Au is sufficient for a complete coverage of the polyhedron whereas it cannot entirely cover the cube. Moreover, Au bilayers are preferentially formed on the Fe(100) faces of the cube before a complete coverage of the corners and edges is achieved. From N_{at}^{Au}/N_{at}^{Fe} reaching ≈0.6, the energy of the cubic-core NP becomes lower than that of the Wulff-core NP and remains as such for higher amounts of Au. This corresponds to the growth stage when the cube is completely covered by gold and points to the higher

stability of the cubic-core NP with respect to the Wulff-core NP for Au shells thicker than ≈2 monolayers in our model. Finally, as the ratio N_{at}^{Au}/N_{at}^{Fe} exceeds approximately 0.8, the two curves increase concomitantly for both types of iron core shapes, NPs with a cubic core exhibiting a lower energy than those based on the Wulff core.

In summary, when Au atoms are deposited on a Fe core, the most stable form of the Fe-Au NPs evolves from a core-shell structure with a Wulff-like polyhedron core and a uniformly distributed Au shell towards a symmetrical core-shell structure with a cubic-like core and truncated square Au pyramids on each of the 6 facets. The crossover between the two shapes occurs when there is enough gold to form at least two monolayers.

This result is in remarkable agreement with the experimental observations of Ref. 31 which showed a different equilibrium morphology of Fe-Au nanoparticles when the amount of Au is low or high with respect to that of Fe. These NPs were obtained by sequential deposition, Fe NPs being produced first on a silica or alumina substrate before depositing gold. Kamp *et al.*[33] have also observed the formation of such core-shell Fe@Au nanoparticles with a cubic Fe core and Au truncated pyramids after high temperature annealing of spherical NPs first obtained by laser ablation in liquid.

The present results should be understood as illustrating equilibrium properties, and do not directly provide information about the barrier that the core-shell particle with a polyhedral core needs to cross to transform into another core-shell particle but with a cubic core. The MC simulations performed at 800 K did not yield any such shape transition of the core, even though the iron atoms were perfectly allowed to rearrange as well. Simulations were also attempted at higher temperatures, but these resulted in the Au shell to melt before the desired transition was achieved. We thus deduce from such numerical experiments that the energy barrier to be crossed must be relatively high, and that enhanced sampling of the energy landscape would be needed to characterize the barriers and overall mechanisms in greater details.

4 Fe-Ag nanoparticles

The variations of the energies per atom as a function of the number of added silver on the two types of Fe cores are shown in Fig. 7. As was the case for Fe-Au, at very low amounts of silver the growth necessarily starts with the Wulff Fe core which is significantly more stable than the cubic core, in the limit of low amounts of noble metal. However, in contrast to the Fe-Au case, the evolution of the two curves is similar in the explored region of Ag/Fe ratio reaching as high as $N_{at}^{Ag}/N_{at}^{Fe} = 2.25$.

Configurations taken along the growth pathways are depicted in Figs. 8 and 9 for particles based on the Wulff and cubic Fe cores, respectively.

In the case of the Wulff core, the Ag atoms start by forming a bilayer on one hemisphere of the polyhedron (configuration **1** in Fig. 8), then one main pyramid is formed and Ag bilayers develop on neighboring facets of the core (configurations **2** and **3** in Fig. 8). At small silver amounts, the morphology of the Fe-Ag NP is therefore somewhat akin to a Janus one. Eventually the extra Ag atoms form bilayers on the whole surface of the core and begin to

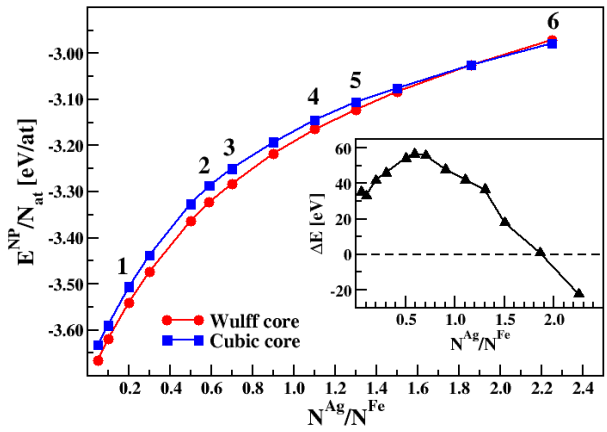

Fig. 7 Evolution of the energy per atom as a function of the N_{at}^{Ag}/N_{at}^{Fe} ratio (for $N_{at}^{Fe} = 1000$), for the two Fe core morphologies: Wulff-like (red circles) and cubic-like (blue squares), after Monte Carlo relaxation at 800 K. Inset: Energy difference (in eV) $\Delta E = E_{cube} - E_{Wulff}$ between the two morphologies.

grow additional pyramids (configurations **4**, **5** and **6** in Fig. 8). As N_{at}^{Ag}/N_{at}^{Fe} exceeds approximately 1.3, the Fe core is totally covered by silver. At larger amounts of Ag ($N_{at}^{Ag}/N_{at}^{Fe} > 1.9$, configuration **6** in Fig. 8), the Fe-Ag nanoparticle still exhibits an off-centered core-shell morphology.

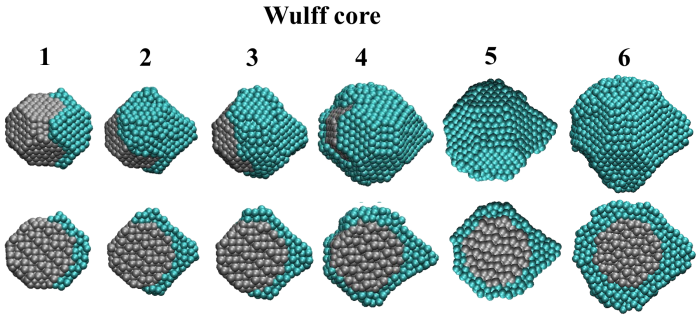

Fig. 8 Selected configurations of the Fe-Ag nanoparticles with a Wulff Fe core, taken along the growth pathway (Fig. 7). Upper panel: outside views; lower panel: back halves shown.

In the cubic core case, the addition of Ag atoms preferentially proceeds over one single facet (configuration **1** in Fig. 9), eventually growing to form one large pyramid before continuing to cover the iron core (configurations **2** and **3** in Fig. 9). The neighboring facets become themselves partially coated when the number of Ag atoms further increases, although the Fe core is never totally covered even for a ratio $N_{at}^{Ag}/N_{at}^{Fe} \approx 1.9$ (configurations **4**, **5** and **6** in Fig. 9). It is interesting to note that, although never fully coated, the morphology of the Fe-Ag nanoparticle with a cubic iron core resembles that of Fe-Au nanoparticles, with truncated pyramids in epitaxial contact with the faces of the cubic core. In addition, we find that the corners of the Fe core that are not covered by Ag are truncated by small Fe(110) facets, which brings the morphol-

ogy of the uncovered core closer to the iron Wulff shape. Finally, it may seem that the cubic core looks more square and defect-free in Fig. 9 than in Fig. 6, but its shape actually did not change and this is merely a consequence of the particles being shown from different viewpoints.

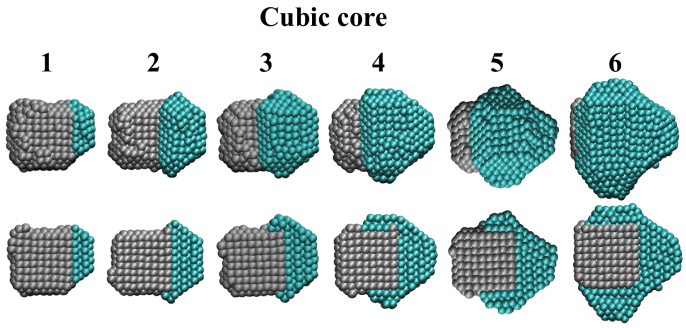

Fig. 9 Selected configurations of the Fe-Ag nanoparticles with a cubic Fe core, taken along the growth pathway (Fig. 7). Upper panel: outside views; lower panel: only back halves shown.

In summary, because of the high interface energy at the origin of the small value of the wetting parameter, the Ag atoms prefer to develop one main pyramid upon deposition on an iron polyhedral core, therefore resembling a Janus-like morphology. Doing so, the nanoparticle limits the energy cost by reducing the interface area and increasing the Ag(111) facets area. Moreover, conversely to the case of Fe-Au, the Fe-Ag NPs with a Wulff core shape are energetically favored over those with a cubic core shape until the Ag amount exceeds about twice the amount of iron. This most probably originates from the higher Fe-Ag interface energies with respect to the Fe-Au ones. Eventually, the cubic core NP becomes more favorable than the Wulff-core one, even with a bare exposed Fe(100) facet, which underlines the particular stability of the truncated pyramids in these systems.

These results partly explain the difficulties often reported in the experimental literature in successfully synthesizing Fe@Ag nanoparticles. It can notably be conceived that if the iron core is not entirely covered by silver, it would remain easily oxidizable.[43] For moderate amounts of silver, the obtained morphology is that of a spherical core-shell with an off-centered core, in complete agreement with the conclusions of Ref. 44. Besides, the dumbbell-like FeAg NPs embedded in Si and as obtained by Benelmekki *et al.*[45] present a Janus-like morphology which is very much alike our Fe-Ag nanoparticles when the amount of Ag is small.

5 Discussion and Conclusion

The deposition of gold or silver on iron nanometric cores having two distinct shapes was computationally modelled, and it was found that the resulting nanoparticles have a radically different morphology depending on the amount and the type of noble metal deposited. These remarkable dissimilarities are mainly due to the difference in the overlaps between the electronic *d* bands of the noble metal (Au or Ag) and those of Fe at the interface, which induces large differences between the energies of the two types of interface considered. This is consistent with the ratio between the two interface energies computed by DFT, which is equal to 1.85 in the Fe-Au system but only to 1.07 in the Fe-Ag system. Our EAM-LJ potential is capable of reproducing these differences between the interface energies. As a consequence, in the present simulations, one of the two interfaces in the Fe-Au system completely disappears, whereas in the Fe-Ag system both interfaces exist and are fairly balanced. This explains why Fe@Au core-shell NPs with a cubic core are found whereas for Fe@Ag polyhedral cores are found. In addition, the interfaces in the Fe-Ag system are energetically more expensive than in the Fe-Au system, which explains why in the first case Janus-type morphologies are observed, while in the second case, core-shell type morphologies with complete wetting are found.

Although the LJ pair potential employed here is highly simplified, it provides a robust description of the main structural features of both Fe-Au and Fe-Ag nanoparticles despite not reproducing all the individual interface energies predicted by DFT with a high accuracy. In the Fe-Au case, the ratio $R_{int}^{Au/Fe}$ between interface energies is higher than the DFT value, and this favors the cubic core shape. However, provided that this ratio is sufficiently large, the transition from the Wulff core shape to the cubic core shape would remain, a lower value of $R_{int}^{Au/Fe}$ simply causing the crossing of the energy curves to occur at higher amounts of gold. Similarly, the magnitude of the wetting parameters S obtained with the LJ potential is too low compared with the DFT data for the Fe-Ag system which results in less efficient wetting but without altering morphological features. Therefore we believe that our models are realistic enough to describe the experimental growth mechanisms rather faithfully.

Additionally, it is fair to recognize that our investigation was not a complete global optimization study, which incidentally would not be feasible for the sizes at stake, but only simulations of the physical growth processes for prescribed core shapes. In particular, because it assumes an already formed core, our modeling could bias the growth towards core-shell or Janus morphologies at the expense of a more mixed alloy. However, the additional Monte Carlo equilibration stages performed after the growth simulations are quite capable of finding an alloy, at least at the interface, if this chemical order had turned out to be the most favorable. Moreover, although this study reveals a change of the stable NPs morphologies with the amount of metal deposited, it does not allow to actually mimic the dynamical evolution of this morphology, nor to account explicitly for various parameters relevant in physical growth such as the collision energy and the deposition rate. Such parameters could be mimicked, in a first approximation, by varying the extent of the intermediate relaxation steps between successive random atom additions. Furthermore, we do not access the intermediate core shapes between the Wulff and the cubic shapes in the Fe-Au system. To do this, enhanced sampling methods should be used in order to explore the transition from the Wulff to the cube core shapes. Work is in progress in this direction.

Finally, the simulations presented here would not be practical to address experimental NP having cores typically larger than 2 to 3 nm,[29–31] i.e. containing millions of atoms or even more. To deal with NPs of such sizes, continuous approaches offer a conve-

nient alternative to the present atomistic simulations, as they can notably predict the equilibrium shape of NPs with a prescribed symmetry from the sole knowledge of the surface and interface energies. Such a model has been constructed very recently for the present core-shell NPs of experimental sizes using for these ingredients the values determined by DFT (Tabs. 1 and 2)[70] and we plan to compare its predictions to the present atomistic results.

To summarize, our computational modeling shows very good agreement with experimental observations for physically grown nanoparticles. In the case of the Fe-Au system, we found an inversion of stability in the core shape when the amount of gold deposited exceeds about two layers, also in agreement with experimental observations.[31] Regarding now Fe-Ag, our results explain the acknowledged difficulty in manufacturing Fe@Ag nanoparticles:[43,44] the iron core is either not fully coated or it is very off-centered and not sufficiently protected from oxidation.

In this work, we showed that a simple additive potential for intermetallic interactions is sufficient to predict morphological transitions in bimetallic core-shell nanoparticles, provided that the surface and interface energies as well as their orderings are properly reproduced. Our computational approach could easily be extended to other core-shell bimetallic systems (and even multimetallic systems) for which an epitaxial relationship exists between the metals of the core and the shell. For example, core-shell FeRh@Au nanoparticles were recently produced[71] and found to exhibit an intermetallic B2-FeRh core surrounded by a faceted Au shell. Our method could be used, e.g. to determine the propensity of such nanoparticles to undergo shape or global transitions with increasing shell thickness. In concern with magneto-plasmonic applications, Fe@AuAg-type nanoparticles could also prove to be extremely efficient[72,73] owing to the possibility to tune the optical response from varying the relative composition in the noble metals. Finally, extensions of the computational methodology are also conceivable towards chemical preparation. For this purpose, the environment could be treated either explicitly (through dedicated potentials) or more semi-empirically by the Monte Carlo growth protocol, e.g. by allowing tailored or swapping moves facilitating reactivity.

Conflicts of interest

There are no conflicts to declare.

Acknowledgements

JL acknowledges financial support of the Fonds de la Recherche Scientifique - FNRS. This work has been performed on the CALMIP computer center (grants n°2018-p1141 and n°2019-p1141). SC, FC and MB thank the GDR CNRS n°3182 "Nanoalliages et nanohybrides à base de métaux" and n°3532 "Modélisation des matériaux" for financial support. Our warm thanks to Joseph Morillo for his MD code and for helpful discussions. MB thanks Nicolas Combe and Nathalie Tarrat for interesting and fruitful discussions and Michèle Benoit for every day support.

Notes and references

1 R. Ferrando, J. Jellinek and R. L. Johnston, *Chemical Reviews*, 2008, **108**, 845–910.

2 P. Chen, K. Murugappan and M. R. Castell, *Physical Chemistry Chemical Physics*, 2020, **22**, 4416–4428.

3 J. Zhao, E. Baibuz, J. Vernieres, P. Grammatikopoulos, V. Jansson, M. Nagel, S. Steinhauer, M. Sowwan, A. Kuronen, K. Nordlund and F. Djurabekova, *ACS Nano*, 2016, **10**, 4684–4694.

4 L. Piccolo, Z. Y. Li, I. Demiroglu, F. Moyon, Z. Konuspayeva, G. Berhault, P. Afanasiev, W. Lefebvre, J. Yuan and R. L. Johnston, *Scientific Reports*, 2016, **6**, 35226.

5 D. Ferrer, A. Torres-Castro, X. Gao, S. Sepúlveda-Guzmán, U. Ortiz-Méndez and M. José-Yacamán, *Nano Letters*, 2007, **7**, 1701–1705.

6 C. Langlois, Z. L. Li, J. Yuan, D. Alloyeau, J. Nelayah, D. Bochicchio, R. Ferrando and C. Ricolleau, *Nanoscale*, 2012, **4**, 3381–3388.

7 D. Nelli and R. Ferrando, *Nanoscale*, 2019, **11**, 13040–13050.

8 A. Mayoral, D. Llamosa and Y. Huttel, *Chemical Communications*, 2015, **51**, 8442–8445.

9 L. Tang, W. Wu, L. He, K. Yu, T. Xu, Q. Zhang, L. Zhang and L. Sun, *The Journal of Physical Chemistry Letters*, 2019, **10**, 1973–1980.

10 T.-W. Liao, A. Yadav, K.-J. Hu, J. van der Tol, S. Cosentino, F. D'Acapito, R. E. Palmer, C. Lenardi, R. Ferrando, D. Grandjean and P. Lievens, *Nanoscale*, 2018, **10**, 6684–6694.

11 G. D. Förster, M. Benoit and J. Lam, *Phys. Chem. Chem. Phys.*, 2019, **21**, 22774–22781.

12 B. Kalska-Szostko, M. Hilgendorff, M. Giersig and P. Fumagalli, *Applied Physics A*, 2013, **111**, 853–859.

13 E. Atmatzakis, N. Papasimakis, V. Fedotov, G. Vienne and N. I. Zheludev, *Nanophotonics*, 2018, **7**, 199–206.

14 N. Bhattarai, G. Casillas, S. Khanal, D. Bahena, J. J. Velazquez-Salazar, S. Mejia, A. Ponce, V. P. Dravid, R. L. Whetten, M. M. Mariscal and M. Jose-Yacaman, *MRS Communications*, 2013, **3**, 177–183.

15 C. Gellini, F. L. Deepak, M. Muniz-Miranda, S. Caporali, F. Muniz-Miranda, A. Pedone, C. Innocenti and C. Sangregorio, *The Journal of Physical Chemistry C*, 2017, **121**, 3597–3606.

16 W. P. Davey, *Physical Review*, 1925, **25**, 753–761.

17 L. J. Swartzendruber, *Bulletin of Alloy Phase Diagrams*, 1984, **5**, 560–564.

18 H. Okamoto, T. B. Massalski, L. J. Swartzendruber and P. A. Beck, *Bulletin of Alloy Phase Diagrams*, 1984, **5**, 592–601.

19 X. Guo, P. Brault, G. Zhi, A. Caillard, G. Jin and X. Guo, *J. Phys. Chem. C*, 2011, **115**, 24164–24171.

20 N. Ahmadi, R. Poursalehi, A. Kirilyuk and M. K. Moravvej-Farshi, *Applied Surface Science*, 2019, **479**, 114–118.

21 V. Amendola, M. Meneghetti, O. M. Bakr, P. Riello, S. Polizzi, D. H. Anjum, S. Fiameni, P. Arosio, T. Orlando, C. de Julian Fernandez, F. Pineider, C. Sangregorio and A. Lascialfari, *Nanoscale*, 2013, **5**, 5611.

22 J. Lin, W. Zhou, A. Kumbhar, J. Wiemann, J. Fang, E. Carpenter and C. O'Connor, *Journal of Solid State Chemistry*, 2001, **159**, 26–31.

23 S.-J. Cho, S. M. Kauzlarich, J. Olamit, K. Liu, F. Grandjean, L. Rebbouh and G. J. Long, *Journal of Applied Physics*, 2004, **95**, 6804–6806.

24 O. Pana, C. M. Teodorescu, O. Chauvet, C. Payen, D. Macovei, R. Turcu, M. L. Soran, N. Aldea and L. Barbu, *Surface Science*, 2007, **601**, 4352–4357.

25 A. Naitabdi and B. Roldan Cuenya, *Applied Physics Letters*, 2007, **91**, 113110.

26 A. Naitabdi, L. K. Ono, F. Behafarid and B. R. Cuenya, *The Journal of Physical Chemistry C*, 2009, **113**, 1433–1446.

27 M. Chen, S. Yamamuro, D. Farrell and S. A. Majetich, *Journal of Applied Physics*, 2003, **93**, 7551–7553.

28 A. Y. Soloveva, N. K. Eremenko, I. I. Obraztsova, A. N. Eremenko and S. P. Gubin, *Russ. J. Inorg. Chem.*, 2018, **63**, 444–448.

29 C. Langlois, P. Benzo, R. Arenal, M. Benoit, J. Nicolai, N. Combe, A. Ponchet and M. J. Casanove, *Nano Letters*, 2015, **15**, 5075–5080.

30 P. Benzo, M. Benoit, N. Tarrat, C. Langlois, R. Arenal, B. Pécassou, A. L. Priol, N. Combe, A. Ponchet and M. J. Casanove, 2016 IEEE Nanotechnology Materials and Devices Conference (NMDC), 2016, pp. 1–3.

31 P. Benzo, S. Combettes, B. Pecassou, N. Combe, M. Benoit, M. Respaud and M. J. Casanove, *Physical Review Materials*, 2019, **3**, 096001.

32 P. Wagener, J. Jakobi, C. Rehbock, V. S. K. Chakravadhanula, C. Thede, U. Wiedwald, M. Bartsch, L. Kienle and S. Barcikowski, *Scientific Reports*, 2016, **6**, 23352.

33 M. Kamp, A. Tymoczko, U. Schürmann, J. Jakobi, C. Rehbock, K. Rätzke, S. Barcikowski and L. Kienle, *Crystal Growth & Design*, 2018, **18**, 5434–5440.

34 K. Sun, T. Cheng, L. Wu, Y. Hu, J. Zhou, A. Maclennan, Z. Jiang, Y. Gao, W. A. Goddard and Z. Wang, *Journal of the American Chemical Society*, 2017, **139**, 15608–15611.

35 A. Tymoczko, M. Kamp, O. Prymak, C. Rehbock, J. Jakobi, U. Schürmann, L. Kienle and S. Barcikowski, *Nanoscale*, 2018, **10**, 16434–16437.

36 P. Mukherjee, P. Manchanda, P. Kumar, L. Zhou, M. J. Kramer, A. Kashyap, R. Skomski, D. Sellmyer and J. E. Shield, *ACS Nano*, 2014, **8**, 8113–8120.

37 J. Vernieres, S. Steinhauer, J. Zhao, A. Chapelle, P. Menini, N. Dufour, R. E. Diaz, K. Nordlund, F. Djurabekova, P. Grammatikopoulos and M. Sowwan, *Advanced Functional Materials*, 2017, **27**, 1605328.

38 J. Vernieres, S. Steinhauer, J. Zhao, P. Grammatikopoulos, R. Ferrando, K. Nordlund, F. Djurabekova and M. Sowwan, *Advanced Science*, 2019, 1900447.

39 K. J. Carroll, D. M. Hudgins, S. Spurgeon, K. M. Kemner, B. Mishra, M. I. Boyanov, L. W. Brown, M. L. Taheri and E. E. Carpenter, *Chemistry of Materials*, 2010, **22**, 6291–6296.

40 L. Lu, W. Zhang, D. Wang, X. Xu, J. Miao and Y. Jiang, *Materials Letters*, 2010, **64**, 1732–1734.

41 M. N. Nadagouda and R. S. Varma, *Crystal Growth & Design*, 2007, **7**, 2582–2587.

42 K. Sridharan, T. Endo, S.-G. Cho, J. Kim, T. J. Park and R. Philip, *Optical Materials*, 2013, **35**, 860–867.

43 J. Ramade, N. Troc, O. Boisron, M. Pellarin, M.-A. Lebault, E. Cottancin, V. T. A. Oiko, R. C. Gomes, V. Rodrigues and M. Hillenkamp, *Nano Research*, 2018, **11**, 6074–6085.

44 J. Ramade, E. Cottancin, M.-A. Lebeault, C. Langlois, L. Piccolo, M. Broyer, M. Hillenkamp, J. Lermé, F. Calvo and M. Pellarin, *The Journal of Physical Chemistry C*, 2019, **123**, 15693–15706.

45 M. Benelmekki, M. Bohra, J.-H. Kim, R. E. Diaz, J. Vernieres, P. Grammatikopoulos and M. Sowwan, *Nanoscale*, 2014, **6**, 3532–3535.

46 Z. Marková, K. M. Šišková, J. Filip, J. Čuda, M. Kolář, K. Šafářová, I. Medřík and R. Zbořil, *Environmental Science & Technology*, 2013, **47**, 5285–5293.

47 F. Calvo, N. Combe, J. Morillo and M. Benoit, *The Journal of Physical Chemistry C*, 2017, **121**, 4680–4691.

48 G. Kresse and J. Furthmüller, *Phys. Rev. B*, 1996, **54**, 11169–11186.

49 G. Kresse and D. Joubert, *Phys. Rev. B*, 1999, **59**, 1758–1775.

50 J. P. Perdew, K. Burke and M. Ernzerhof, *Phys. Rev. Lett.*, 1996, **77**, 3865–3868.

51 X. W. Zhou, R. A. Johnson and H. N. G. Wadley, *Physical Review B*, 2004, **69**, 144113.

52 W. R. Tyson and W. A. Miller, *Surface Science*, 1977, **62**, 267 – 276.

53 F. R. De Boer, R. Boom, W. C. M. Mattens, A. R. Miedema and A. K. Niessen, *Cohesion in Metals: transition metal alloys*, North-Holland, Amsterdam, 1989, vol. 1.

54 Y. Saito, *Journal of Crystal Growth*, 1981, **53**, 273–279.

55 S. Giorgio, C. Henry, C. Chapon, G. Nihoul and J. Penisson, *Ultramicroscopy*, 1991, **38**, 1–12.

56 A. R. Miedema, *Z. Metallkunde*, 1978, **69**, 287.

57 S. Stankic, R. Cortes-Huerto, N. Crivat, D. Demaille, J. Goniakowski and J. Jupille, *Nanoscale*, 2013, **5**, 2448.

58 M. Benoit, C. Langlois, N. Combe, H. Tang and M.-J. Casanove, *Phys. Rev. B*, 2012, **86**, 075460.

59 M. Benoit, N. Combe, A. Ponchet, J. Morillo and M.-J. Casanove, *Phys. Rev. B*, 2014, **90**, 165437.

60 E. Bauer and J. H. van der Merwe, *Physical Review B*, 1986, **33**, 3657–3671.

61 S. Lu, Q.-M. Hu, M. P. J. Punkkinen, B. Johansson and L. Vitos, *Physical Review B*, 2013, **87**, 224104.

62 P. A. Fatematossadat, M. Mohammadi and S. E. Roozmeh, *Journal of Molecular Graphics and Modelling*, 2019, **90**, 33–41.

63 N. Bartlett, *Gold Bulletin*, 1998, **31**, 22–25.

64 H. Chamati, N. Papanicolaou, Y. Mishin and D. Papaconstantopoulos, *Surface Science*, 2006, **600**, 1793–1803.

65 M. I. Mendelev, S. Han, D. J. Srolovitz, G. J. Ackland, D. Y. Sun and M. Asta, *Philosophical Magazine*, 2003, **83**, 3977–3994.

66 P. L. Williams, Y. Mishin and J. C. Hamilton, *Modelling and Simulation in Materials Science and Engineering*, 2006, **14**, 817–833.

67 H. Chamati and N. I. Papanicolaou, *Journal of Physics: Condensed Matter*, 2004, **16**, 8399–8407.
68 H. Akbarzadeh, E. Mehrjouei, A. N. Shamkhali, M. Abbaspour, S. Salemi and M. Kamrani, *New Journal of Chemistry*, 2018, **42**, 9666–9675.
69 M. Nathanson, K. Kanhaiya, A. Pryor, J. Miao and H. Heinz, *ACS Nano*, 2018, **12**, 12296–12304.
70 A. Ponchet, S. Combettes, P. Benzo, N. Tarrat, M. J. Casanove and M. Benoit, *Journal of Applied Physics*, 2020, **128**, 055307.
71 P. Benzo, S. Combettes, C. Garcia, T. Hungria, B. Pécassou and M.-J. Casanove, *Crystal Growth & Design*, 2020, acs.cgd.0c00414.
72 H. Yao and T. Shiratsu, *Journal of Nanophotonics*, 2020, **14**, 1.
73 G. A. Sotiriou, G. D. Etterlin, A. Spyrogianni, F. Krumeich, J.-C. Leroux and S. E. Pratsinis, *Chem. Commun.*, 2014, **50**, 13559–13562.